

On-Chip Super-Resolution Imaging with Fluorescent Polymer Films

Chenlei Pang, Jingxi Li, Mingwei Tang, Jianpu Wang, Ioanna Mela, Florian Ströhl, Lisa Hecker, Weidong Shen, Qiulan Liu, Xiaowei Liu, Yinan Wang, Hao Zhang, Meng Xu, Xinghong Zhang, Xu Liu,* Qing Yang,* and Clemens F. Kaminski

Wide field-of-view (FOV), label-free, super-resolution imaging is demonstrated using a specially designed waveguide chip that can illuminate a sample with multicolor evanescent waves travelling along different directions. The method is enabled by a polymer fluorescent film that emits over a broad wavelength range. Its polygonal geometry ensures coverage over all illumination directions, enabling high-fidelity image reconstruction while minimizing distortion and image blurring. By frequency shifting and iterative stitching of different spatial frequencies in Fourier space, the reconstruction of 2D samples is achieved without distortion over wide FOVs. The fabrication process is facile and compatible with conventional semiconductor-fabrication methods. The super-resolution chip (SRC) can thus be produced with high yield, offering opportunities for potential conjunction of super-resolution techniques integrated optical circuits or for the development of single-use diagnostic kits.

microscopy (PALM),^[4,5] structured illumination microscopy (SIM),^[6,7] and stochastic optical reconstruction microscopy (STORM)^[8–10] have demonstrated improved spatial resolution to less than 30 nm, leading to breakthrough discoveries in the life sciences. However, these methods are incoherent imaging techniques and rely on the use of fluorescent labels. This prevents their use for dynamic, label-free imaging, for example, in studies of the movement of subcellular organelles or in nonbiological applications, such as chip and materials inspection. To complement the various far field super-resolution imaging methods based on fluorescence, various label-free, coherent imaging techniques have been


1. Introduction

Optical microscopy at high resolution plays an indispensable role in many areas of research, including biology, device fabrication, and materials research. However, in conventional microscopy, the attainable resolution is limited to around half the wavelength of the illumination light. To overcome this limit, various methods of far-field super-resolution microscopy have been reported over the past decades. Fluorescence-based super-resolution techniques such as stimulated emission depletion (STED) microscopy,^[1–3] photoactivated localization

developed. They are based on the scattering of evanescent waves by the sample and the designed imaging components to capture high spatial frequency information. Examples include the hyperlens,^[11–14] microsphere contacting,^[15–17] microfiber illumination,^[18] and nanowire ring illumination^[19,20] methods, all of which with capability of resolving subwavelength information. The techniques mentioned have potential for integration with engineered substrates which can be used in conjunction with conventional brightfield microscopes. However, the acquired images of the sample by these techniques are enlarged with different magnification factor depending on their real size

C. L. Pang, J. X. Li, M. W. Tang, Prof. W. D. Shen, Q. L. Liu, Dr. X. W. Liu, Y. N. Wang, Prof. X. Liu
State Key Laboratory of Modern Optical Instrumentation
College of Optical Science and Engineering
Zhejiang University
Hangzhou 310027, China
E-mail: liuxu@zju.edu.cn

Prof. J. P. Wang, H. Zhang, M. Xu
Institute of Advanced Materials
Nanjing Tech University
Nanjing 211816, China

 The ORCID identification number(s) for the author(s) of this article can be found under <https://doi.org/10.1002/adfm.201900126>.

© 2019 The Authors. Published by WILEY-VCH Verlag GmbH & Co. KGaA, Weinheim. This is an open access article under the terms of the Creative Commons Attribution License, which permits use, distribution and reproduction in any medium, provided the original work is properly cited.

The copyright line was changed on 29 May 2019 after initial publication.

DOI: 10.1002/adfm.201900126

Dr. I. Mela, Dr. F. Ströhl, L. Hecker, Prof. C. F. Kaminski
Department of Chemical Engineering and Biotechnology
University of Cambridge
Cambridge CB3 0AS, United Kingdom

Prof. X. H. Zhang
MOE Key Laboratory of Macromolecular Synthesis and Functionalization
Department of Polymer Science and Engineering
Zhejiang University
Hangzhou 310027, China

Prof. Q. Yang
State Key Lab. of Modern Optical Instrumentation
College of Optical Science and Engineering
Zhejiang University
Hangzhou 310027, China
E-mail: qingyang@zju.edu.cn

Prof. Q. Yang
Collaborative Innovation Center of Extreme Optics
Shanxi University
Taiyuan 030006, China

and structures, suffering from serious distortions. In addition, because of the lack of precise control on evanescent illumination direction, these techniques suffer from frequency-aliasing and it is impossible for them to recover the original sizes of the samples. Fluorescence based super-resolution techniques have also been used in conjunction with waveguides chips,^[21–25] demonstrating the potential of integrating photonic circuit technologies with super-resolution imaging. However, the label-free coherent imaging on chip without distortion and blurring has not so far been reported. The design of an integrated chip for label-free, far field, super-resolution imaging would thus present a significant advance for a broad range of applications.

Here, we first introduce a super-resolution chip (SRC) capable of generating high wave vector components in the evanescent wave illumination to enable label-free, super-resolution imaging in a wide field microscope. By integrating an improved image reconstruction algorithm into our SRC-based illumination, we demonstrate that our approach effectively eliminates the image blurring and distortion artifacts which plagued previous implementations of evanescent wave imaging.^[11–20] We show that we can image 2D structures containing multiple spatial frequency components in arbitrary directions at subwavelength resolution. An essential component of our approach is the patterning of our SRC with poly(9,9'-dioctylfluorene-alt-benzothiadiazole) (F8BT) molecules, which are widely used in organic light emitting diode (OLED). Compared with microfiber and nanowire light sources, the fluorescent polymer films have superior luminescence and cost efficiencies, they are facile to fabricate, and scale-up for mass production is feasible.^[26–31] The wideband fluorescence emission of F8BT (from 480 to 700 nm for excitation in the blue) covers a large spatial frequency range, which is vital for the reconstruction distortion free images from the sample.^[32–35]

In this work, we etched the F8BT film on a glass substrate with different polygonal shapes. The film was excited monochromatically at different locations, to generate

illumination fields with multiple wave vector components. The emitted photons are waveguided along different directions of the film providing omnidirectional illumination. Vertical and oblique illumination are also applied to illuminate the sample, making sure enough coverage of frequency information from low frequency range to high frequency range. This enabled the distortion free, subwavelength resolution imaging of the sample in the center of the working region. Iterative algorithm was used to reconstruct images in Fourier space and well-converging solutions were obtained. The obtained results agreed well with scanning electron microscopy (SEM) and atomic force microscopy (AFM) images obtained from the same sample.

2. Results and Discussion

2.1. Imaging Principle

Figure 1a demonstrates the fabrication procedures for SRCs to produce evanescent waves at multiple wavelengths/directions. When a sample $o(r)$ with subwavelength size features is illuminated by an evanescent light with a wave vector K_{eva} , the scattered light can be written as $s(r) = o(r)\exp(iK_{\text{eva}} \cdot r)$. Here, $r = (x, y)$ refers to the coordinates in the spatial domain. The detected intensity image of the target is given by Equation (1):

$$I(r) = \left| F^{-1} \left(O(K - K_{\text{eva}}) \times H(K) \right) \right|^2 \quad (1)$$

where $O(K) = F(o(r))$ is the Fourier spectrum of the sample and $H(K) = F(h(r))$ is the optical transfer function (OTF) of the microscope system, $K = (K_x, K_y)$ is the coordinate in the spatial frequency domain. The spatial frequencies of the samples are thus shifted to new frequencies $K' = K - K_{\text{eva}}$ under evanescent wave illumination. Information of the sample is only collected

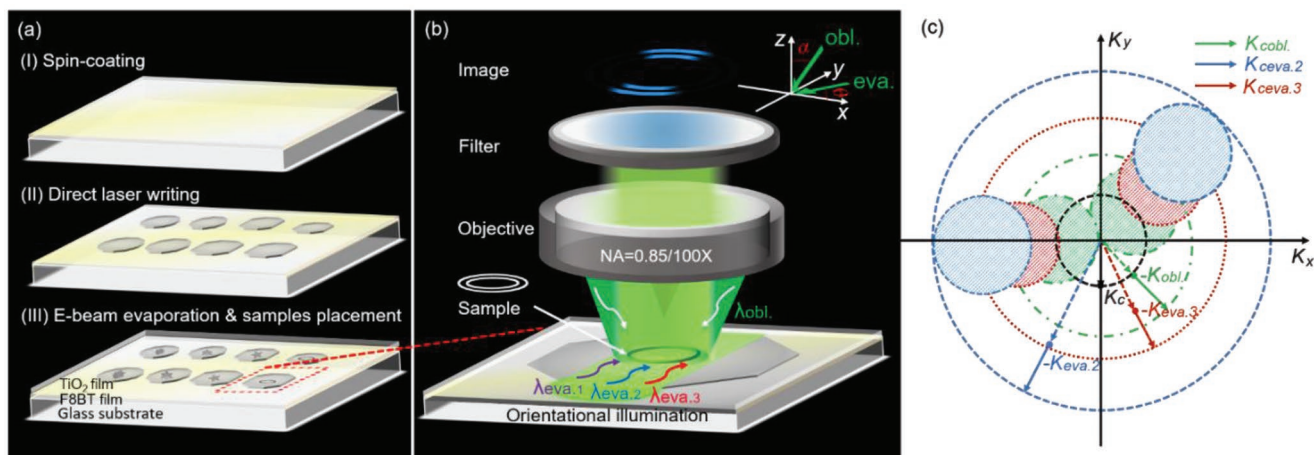


Figure 1. a) Fabrication procedures for SRCs to produce evanescent waves at multiple wavelengths/directions. b) Schematic diagram of the evanescent field illumination and oblique illumination process. Under a given illumination direction, the object (here a circular ring pair) is partially resolved at different wavelengths using appropriate bandpass filters. In the diagram, θ represents the illumination direction and α is the incidence angle for oblique illumination. And obl. means oblique illumination, eva. represents evanescent illumination. c) Schematic of reconstruction method. K_c , $K_{\text{cobl.}}$, $K_{\text{ceva.2}}$, and $K_{\text{ceva.3}}$ are the cut-off wavenumbers of the microscope system for different illumination modes and wavelengths; $K_{\text{obl.}}$ is the wave vector under oblique illumination; $K_{\text{eva.2}}$ and $K_{\text{eva.3}}$ are wave vectors for evanescent field illumination at wavelengths of λ_2 and λ_3 , respectively.

for $|K'| < |K_c|$ where $K_c = K_0 \times NA = 2\pi NA/\lambda_0$ is the cut-off wavenumber of the microscope system, λ_0 is the vacuum wavelength of the illumination light.

For subwavelength label-free, super-resolution imaging,^[11–20] because of the loss of spatial frequency information, the acquired images suffer from serious distortion. Widening the spatial frequency spectrum and illumination from multiple directions are key to successful reconstruction without distortion. In contrast to previous work, our chip design has the following advantages. First, we introduced multiple directions in the illuminating wave vectors to induce multiangle frequency shifting. Second, signals can be collected under a variety of illumination conditions and at different wavelengths, extending the spatial frequency information accessible from the sample. Figure 1b illustrates the unidirectional evanescent waves illumination originating from an individual side of the polygon: when a localized F8BT region is excited, the broadband fluorescence emission is confined within the planar waveguide and propagates toward the center of the polygonal region. The fields interact with the sample to produce scattered light, which is then imaged in the far field through a bandpass filter for frequency selection. Changing the excitation location along the edge of the polygon region, multiple illumination angles are produced, enabling 2D imaging.

Furthermore, oblique and vertical illumination (i.e., non-evanescent fields) is also performed to further extend the range of illumination wave vectors (Figure 1b; Figure S6, Supporting Information). Figure 1c illustrates how such illuminations are used to map out extended regions in K space to resolve subwavelength details. Conventional vertical illumination is used to transmit the low frequency information for imaging. Evanescent illumination waves of different wavelengths shift different high frequency components of the sample into the passband of the microscope system. The oblique illumination connects the low and high frequency ranges. Wavelength variation and different illumination modes thus ensure that there are no empty regions in K space. By iteratively stitching together the acquired frequency components, a converged frequency distribution $F(K_x, K_y)$ is restored in Fourier space. Finally, using inverse Fourier transformation, the converged solution is transformed back to the spatial domain to recover a super-resolved image of the sample^[36–43] (Figure S7, Supporting Information).

2.2. Results from Simulations

Precise control of excitation conditions and unidirectional propagation properties of the waveguide structure are key factors to the success of the technique. As demonstrated in Figure S8, Supporting Information, when the light field is injected into a hexagon planar waveguide from one side, the propagating light field is predominantly confined to a narrow range of angles. Figure 2a shows simulation results for a pair of concentric circles with radii differing by 160 nm (80 nm linewidth and 80 nm gap width). The wavelengths for vertical and oblique illumination modes was modeled to be at 520 nm; and 532 and 632.8 nm for the evanescent wave illumination, respectively. These illumination conditions were also used for

subsequent experiments presented. The incident angle α for oblique illumination was 60°. As shown in Figure 2b, under oblique illumination, the circle ring pair remains unresolved. Figure 2c shows the corresponding image under evanescent wave illumination at 532 nm with $\theta = 90^\circ$ illumination direction. Clearly, some useful subwavelength information is recovered, however only along the illumination direction. To reconstruct 2D patterns, the illumination needs to be applied over different incident angles and directions. Figure 2d–f shows the reconstruction results when the number of illumination direction N is 12, 16, or 24, and both oblique and evanescent illumination modes are applied. From the simulation results, $N \geq 16$ suffices to recover the sample information in sufficient detail.

Wide spatial frequency coverage is important to eliminate blurring and distortion in the reconstructed image. Figure 2g shows an array of lines (80 nm linewidth) arranged in the shape of a fan. Figure 2h,i presents the results when the lines are illuminated from 16 directions. The line array was well reconstructed when vertical, oblique, and evanescent wave illumination were presented at different wavelengths (Figure 2h). In contrast, when the evanescent wave illumination at 532 nm was not applied, there was a serious blurring and distortion in the red rectangle region in Figure 2i.

2.3. Experimental Results

To validate our method experimentally, we fabricated a set of three linear trenches (85 nm linewidth, 85 nm spacing, and 70 nm depth) using focused ion beam (FIB) etching on the surface of the titanium dioxide film waveguide (Figure 3a). As demonstrated in Figure 3b,c, the sample is not resolved under vertical and oblique illumination, alone. Next, we illuminated the dye films on those sides of the etched polygon that were parallel to the trench structure. The back scattered signal was filtered through a bandpass filter at 500 ± 2 nm (FWHM = 10 ± 2 nm) or 632.8 ± 2 nm (FWHM = 10 ± 2 nm) for imaging. Polarizer angle was arranged to be parallel with the trenches. Figure 3d,g is images obtained for evanescent wave illumination at these wavelengths. Obviously, no individual illumination mode on its own suffices to recover the components of the pattern. After acquisition, intensity images were aligned using the edge of the polygon region as reference and cropped to the same size for reconstruction. Frequency information in the images was shifted to the correct position in the passband of objective according to the illumination wave vectors before image reconstruction. For oblique illumination, frequency shift vectors were given by $K_{obl.} = (-K_0 \sin \alpha \cos \theta, -K_0 \sin \alpha \sin \theta)$. For the evanescent wave illumination, the shift vectors were determined using the finite-difference time-domain (FDTD) method (see Table S1, Supporting Information). After ten iterations of the recursive process, a wide frequency spectrum of the trenches was recovered (Figure 3h). The spatial frequency spectrum was then processed using an inverse Fourier transform to create the image in the spatial domain and the result is shown in Figure 3i. The line pattern is clearly resolved in the resulting image. Figure 3j shows intensity profiles along

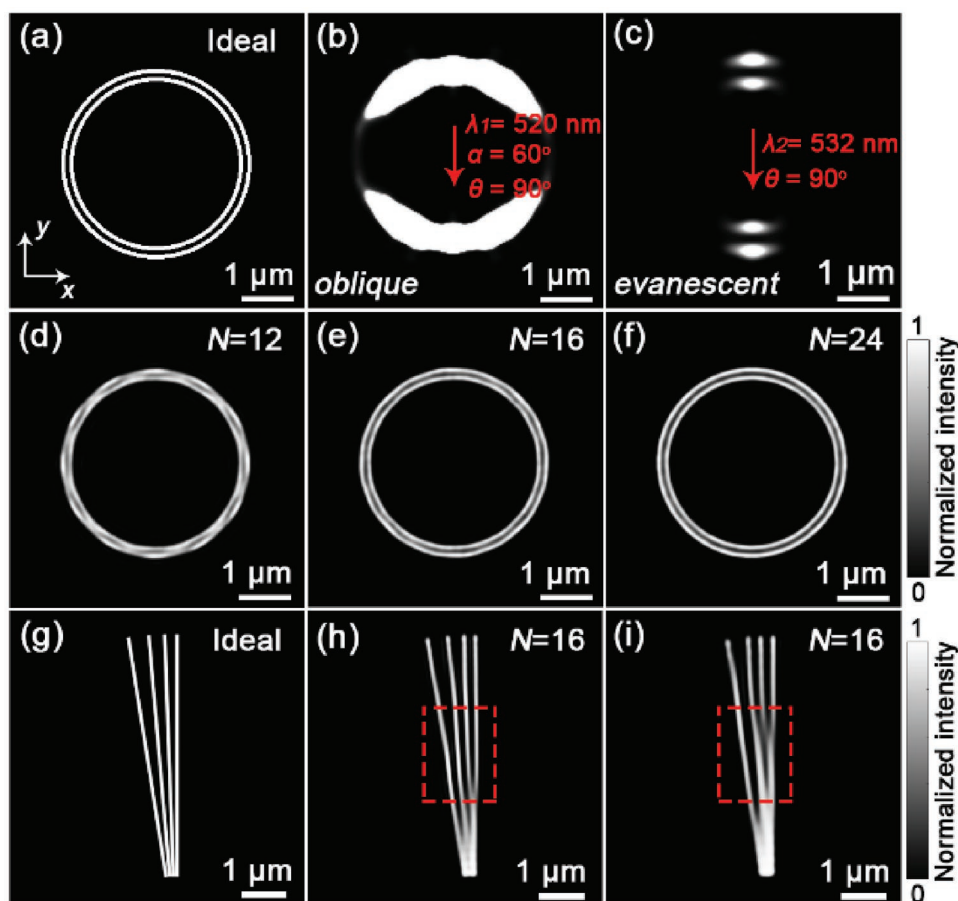


Figure 2. a) Simulated test pattern comprising two concentric rings (80 nm linewidth and 80 nm gap width). b) Simulated image of ring pattern under oblique illumination, with light incident at $\alpha = 60^\circ$ with respect to the chip surface and travelling along a direction defined by the red arrow ($\theta = 90^\circ$). c) Corresponding image for evanescent wave illumination ($\theta = 90^\circ$). d–f) Reconstruction of the double ring pattern for illumination along multiple angular directions including both oblique and evanescent wave illumination. The number of illumination directions $N = 12, 16,$ and 24 , respectively (12, 16, and 24 divisions of 360°). g) Simulated shape containing a line array (80 nm linewidth). From left to right, angles between adjacent lines were $4^\circ, 3^\circ,$ and 2° , respectively. h) Reconstruction for oblique, central, and evanescent wave illumination. i) Reconstruction result for the case where the evanescent wave illumination at 532 nm is omitted.

the white dashed lines indicated in Figure 3a,i and demonstrates good agreement between our experimental result and an SEM image. Simulations showed a good reconstruction fidelity also if the numbers of trenches were increased (Figure S9b–d, Supporting Information). For comparison, if data from the evanescent wave illumination at 632.8 nm was removed from the reconstruction process, the algorithm did not converge and the reconstructed image suffered serious blurring (Figure S9a, Supporting Information).

We next continued to demonstrate the method on more complex samples, containing multiple spatial frequencies along different directions. We produced a sample by engraving the Chinese character for “light,” rendered by a set of parallel trenches to form different line segments of the symbol. The symbol was etched within a hendecagonal working region using the FIB technique (Figure S10a, Supporting Information). As depicted in Figure 4a, the center-to-center distance between etched trenches is 146 nm (76 nm linewidth and 70 gap width) and the profile depth is 70 nm. As these feature sizes were smaller than the diffraction limit, the pattern could

not be resolved by conventional microscopy (Figure 4b). When the pattern was illuminated under oblique illumination at an incident angle of 62.26° from six different directions in step sizes of 60° , the parallel lines in the symbol remained unresolved (Figure S11a–c, Supporting Information). Figure S12d,e, Supporting Information, was obtained using 360° evanescent illumination when the F8BT film around the sample region was fully illuminated by a xenon lamp and scattered signals were detected for two wavelength bands filters at 532 ± 2 nm (FWHM = 10 ± 2 nm) and 632.8 ± 2 nm (FWHM = 10 ± 2 nm). Finally, a 405 nm CW laser source was used to locally excite the F8BT film along different edges of the working region. By exciting the sides and vertex positions of the hendecagon region in turn (Figure S10b–d, Supporting Information), evanescent fields from 22 directions were produced at the two wavelengths (Figure S11f–o, Supporting Information). The polarization angle of the polarizer was changed to perpendicular to corresponding illumination directions. As shown in Figure S11f–o, Supporting Information, the best resolution was obtained only along those directions that were parallel to the illumination direction.

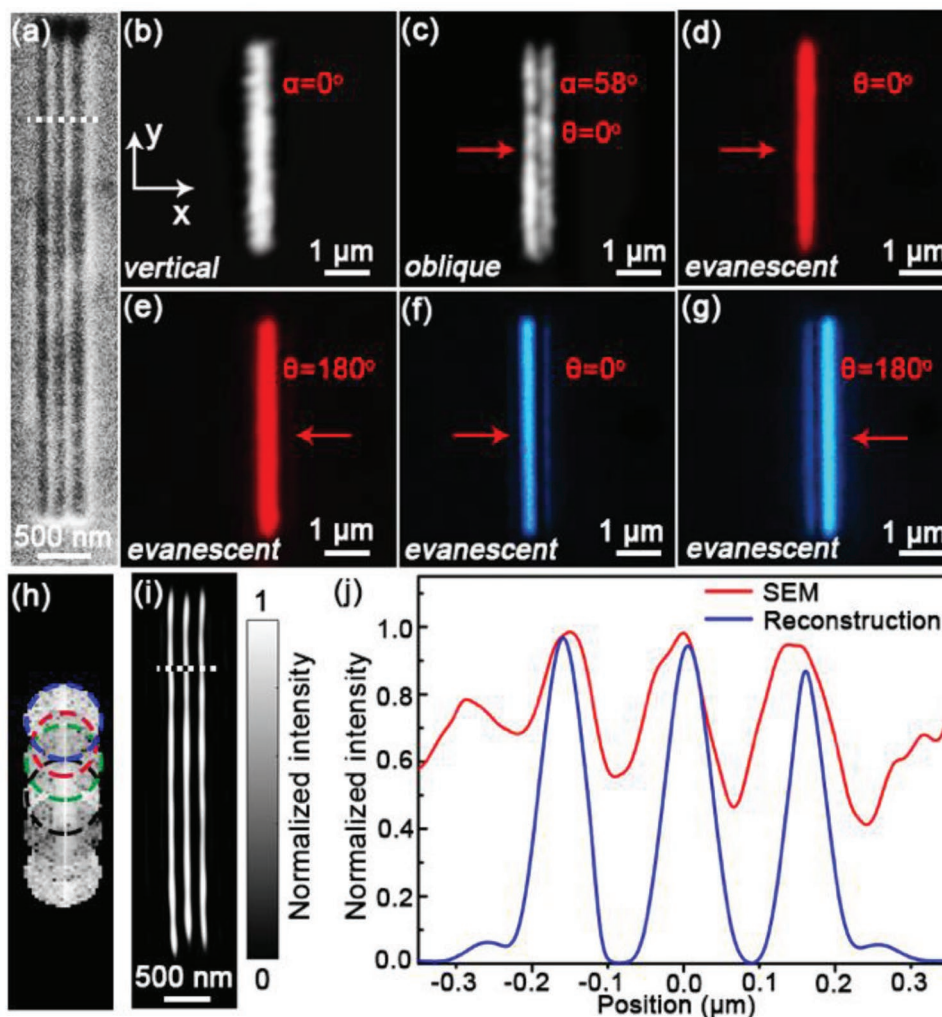


Figure 3. a) SEM image of a structure containing three linear trenches. The center-to-center distance between adjacent trenches is 170 nm (85 nm linewidth and 85 nm gap width); their depth is 70 nm. b) Optical image of structure obtained under vertical illumination. c) Image for oblique illumination with an incidence angle of 58° . d,e) Images under evanescent wave illumination at a wavelength of 632.8 nm. f,g) Evanescent wave illumination at 500 nm. The red arrows represent corresponding propagation directions of illumination waves with respect to the sample surface. h) Frequency spectrum (on a logarithmic scale) of sample image after ten iterations of the frequency reconstruction algorithm. Components within the black, green, red, and blue circles correspond to intensity images under vertical, oblique, and evanescent wave illumination at 532 and 632.8 nm, respectively. i) Final, reconstructed image. j) Normalized intensity profiles corresponding to the dashed lines in Figure 3a,i.

Frequency components carried by the intensity images under different illumination angles were shifted to their correct positions according to the different illumination modes to recover the 2D spatial frequency spectrum for reconstruction. Figure 4c shows the frequency spectrum of the character after ten computational iterations. Performing an inverse Fourier transform on the frequency spectrum yields a well-reconstructed image of the symbol (Figure 4d). FOV of the imaging system is determined by the overlapping region of light fields propagating from different directions. As demonstrated in Figure S10b–d, Supporting Information, length of the side is about $15\ \mu\text{m}$, effective FOV of the system is larger than $200\ \mu\text{m}^2$. Images reconstructed from data without oblique illumination do not match the original pattern well (Figure S12a, Supporting Information). Reducing the number of illumination directions to ten resulted in loss of fidelity, and some details were not well

reconstructed (Figure S12b, Supporting Information). An AFM image of the character shows that the edges of the etched trenches were not homogeneously flat (Figure 4,d,e), which may explain the nonuniformity in parts of the reconstruction results. Even so, normalized intensity profiles agree well between reconstruction result and AFM/SEM images with similar center-to-center distances measured for all three methods (Figure 4g).

To demonstrate the practical capabilities of our SRC to image irregular samples, we deposited bundles of multiwall carbon nanotubes (MWCNTs) (diameter: 10–20 nm; length: 200–250 μm) on the waveguide surface. The sample was illuminated with evanescent waves at wavelengths of 532 nm and 632.8 nm from 16 directions. The samples were produced by dispersing MWCNTs homogeneously in a pure alcohol solution using ultrasonication. The solution was then dripped on the surface

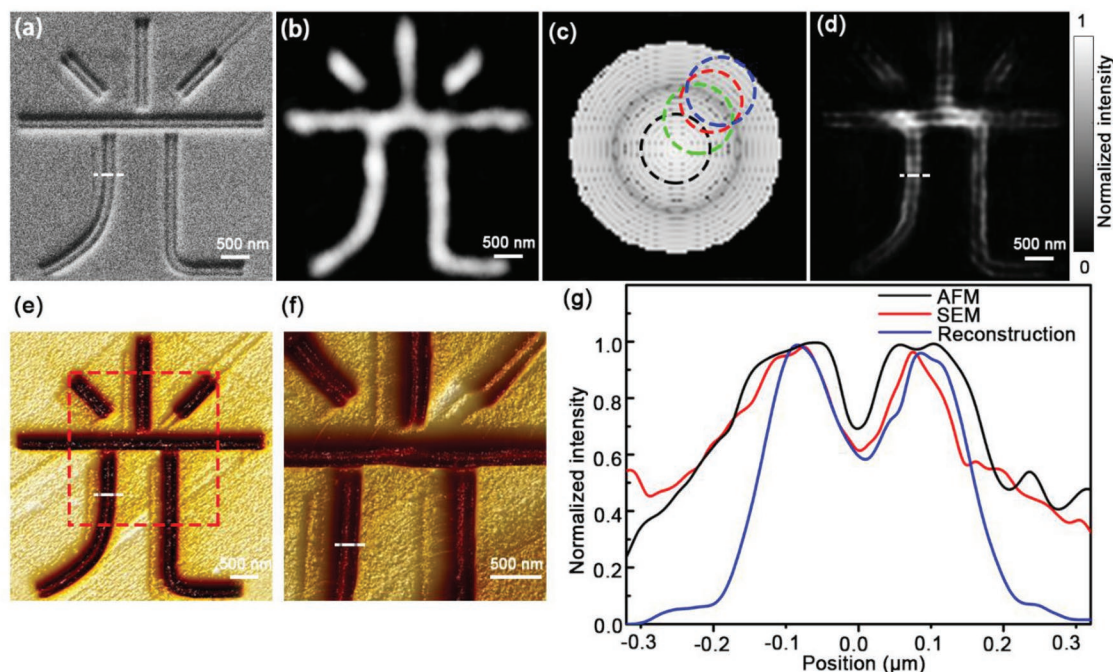


Figure 4. a) SEM image of the Chinese character of “light” etched onto the SRC. The center-to-center distance of lines forming each segment of the symbol is 146 nm; their depth is 70 nm. b) Optical images under vertical illumination. c) Frequency spectrum (on a logarithmic scale) after ten reconstruction iterations. Black, green, red, and blue circles denote frequency information recovered from vertical, oblique, and evanescent wave illumination modes at 532 and 632.8 nm, respectively. d) Reconstructed image using all illumination modes. e) AFM image with f) zoom in view shown in panel (f) corresponding to region bounded by the red rectangle in (e). g) Normalized intensity profiles along white dashed lines depicted in Figure 4a,d,e, respectively.

of a clean glass substrate and from there MWCNTs samples were transferred to the working region of the SRC using optical fiber tapers. **Figure 5a** presents an SEM image of MWCNTs sample 1. As demonstrated in **Figure 5b**, subwavelength details in **Figure 5a** are not resolved by conventional brightfield microscopy. **Figure 5c** shows an image of sample 1 under evanescent illumination along the direction of the white arrow at 532 nm, in which some details are already visible. As demonstrated in **Figure 5d**, MWCNTs sample 1 is well reconstructed using our method. However, since the penetration depth of evanescent

waves is limited, samples must be in direct contact with the sample substrate. For the MWCNTs sample, this was not always the case. **Figure 5e** represents an SEM image of MWCNT sample 2, and clearly, some fibers are crossing over others and therefore not in contact with the substrate. Thus, the evanescent illumination mode does not contribute any information to those parts of the sample (**Figure 5g**) and high spatial frequency detail will miss in the reconstruction. **Figure 5h** demonstrates this, and reconstruction of the upper fiber is poor, while much higher resolution is afforded for the lower fiber that is directly

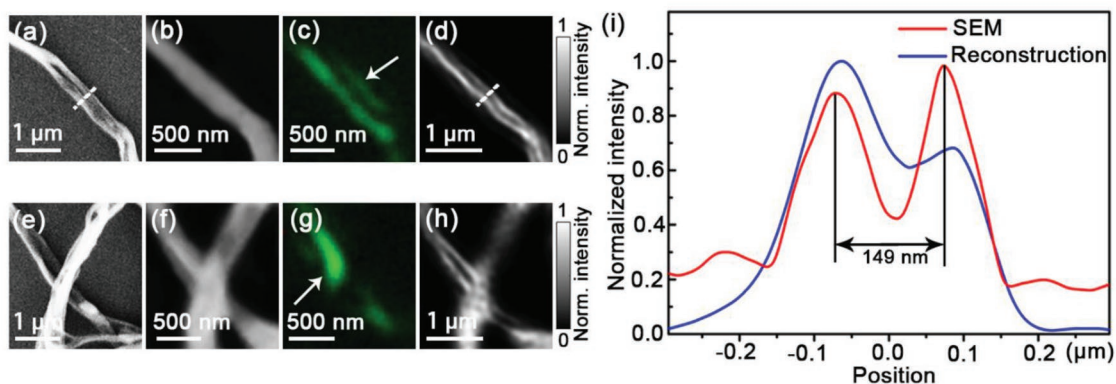


Figure 5. a) SEM image of multiwalled carbon nanotubes (MWCNTs). b) Optical image under vertical illumination. c) Image for evanescent wave illumination at 532 nm along directions of white arrow. d) Reconstructed image using all illumination modes. Panels (e–h) show corresponding images for another sample with two MWCNT strands crossing over one another. Norm. Intensity denotes Normalized intensity. i) Normalized intensity profiles along white dashed lines in (a) and (d).

in contact with the substrate. Intensity profiles are presented in Figure 5i, again demonstrating good agreement between SEM and reconstruction results.

3. Conclusions

In summary, we have demonstrated a novel label-free wide-field SRC that permits convenient illumination of a sample from various directions, incidence angles, and over a large range of wavelengths. In conjunction with a reconstruction algorithm, the technology permits coherent, label-free imaging of samples at subwavelength resolution. Using laser direct writing and E-beam evaporation techniques, polygonal waveguide arrays with different geometries and sizes were manufactured, which were surrounded by F8BT dye films. The latter could be excited locally near a side of the polygonal working region, to emit broad bandwidth fluorescence light, that coupled efficiently into the polygonal waveguide. Through sequential excitation of different sides of the polygon, evanescent waves could be created, travelling toward the sample from different directions. The broad bandwidth evanescent waves scattered by the sample were filtered with narrow band pass filters, to permit sampling of different parts of the spatial frequency spectrum of the sample. By combining the spatial frequency information carried by images under vertical, oblique, and evanescent wave illumination at different wavelengths, high-resolution images of 2D samples were obtained. We demonstrated the methods on subwavelength sized features of etched patterns and MWCNT fibers. Our reconstruction results match well with SEM/AFM images and demonstrate the potential of the SRC for practical applications in material science and in the life science field.

Resolution limit of the technology is determined by wave vectors used for evanescent wave illumination, while quality of the waveguide film determines the propagation distance of the evanescent waves, ultimately limiting the FOV of the system.^[20] As demonstrated in Figure S13, Supporting Information, when the size of the sample is smaller than 40 nm (i.e., the linewidth of a CNT or single etched slot), the full width at half maximum (FWHM) of the normalized intensity profile becomes 128 nm, and we take this to a measure of the system's resolution. In the future, if fluorescence materials with wider spectra than F8BT (e.g., to cover 400–750 nm) and high-quality film waveguides with higher refractive index than titanium dioxide films are available, further resolution enhancements can be afforded in a wider FOV. In our current design, the SRC is transparent, permitting images to be obtained under vertical and oblique illumination modes, as well in transmission. An exciting future opportunity is presented by the possibility to excite the F8BT films by electron injection. Electrodes with given shapes and sizes could be designed to obviate the need for external excitation laser light, making the imaging system more compact and efficient.^[44–47] The penetration depth of evanescent waves into the sample is given by Equation (2):

$$d = \frac{\lambda}{2\pi} \frac{1}{\sqrt{n_{\text{eff}}^2 - n_s^2}} \quad (2)$$

where n_{eff} is the effective mode index of the waveguide mode, and n_s is the refractive index of the sample. In future work, by designing chips with optimized refractive index and thickness, penetration depths of more than a micrometer are conceivable.^[23,48]

4. Experimental Section

Fabrication of a SRC: A 90 nm thick F8BT film was spin-coated on the surface of a 0.5 mm thick, 1.5 cm × 1.5 cm K9 substrate and dried using a heating stage at 80 °C for 5 min. Next, laser direct writing technique was used to fabricate an array of polygonal patterns. Wavelength of the pulsed laser was 780 nm, and its duration time was less than 120 fs with a repetition rate of 80 MHz. Measured laser power was about 310 mW, and machining precision of the system was smaller than 100 nm. Then a 70 nm thick titanium dioxide film was deposited by electron-beam (E-beam) evaporation at room temperature to form a planar waveguide on the glass substrate (Figure S1, Supporting Information). Refractive index of the deposited titanium dioxide film was 2.05.

Characteristics of the Film: AFM was used to verify that the film surface was smooth, and that no fractures were present at the edges of the polygons (Figure S3, Supporting Information). This ensured that fluorescence from the F8BT film (Figure S2, Supporting Information) was coupled efficiently into the titanium dioxide film waveguide. Figure S4 in the Supporting Information shows the surface characteristics of the titanium dioxide waveguide and titanium dioxide/F8BT films. The high quality of the films is evident, permitting low-loss propagation of the coupled light. For imaging, samples were placed in the center of a polygonal region.

Imaging Set-Ups: A 100×, 0.85 NA objective lens was used in an upright microscope (Zeiss AXIO A2m) to focus the 405 nm continuous laser light on the edge of the working region for excitation and to collect the scattered light for imaging. The laser beam was cleaned up using a 20 μm diameter pinhole after a 25×, 0.4 NA objective lens to improve the intensity uniformity of the focused spot (Figure S5, Supporting Information). Wavelength selection of the scattered light was realized by means of a band-pass filter placed in front of the detector. In experiments, a rotatable polarizer was installed in front of the CCD camera (Nikon DS-Fi1c) to permit the selection of desired polarization states in the scattered signal, selecting the illumination directions of transverse light that interacts with samples.

Supporting Information

Supporting Information is available from the Wiley Online Library or from the author.

Acknowledgements

The authors would like to thank Dr. Xianzi Dong for the help in laser direct writing, Dr. Haiqing Yuan for the help in fabricating the SRC, and Dr. Wei Wang for the help in FIB etching. The authors would like to acknowledge the support by National Natural Science Foundation of China (No. 61735017, 61822510, 51672245), Zhejiang Provincial Natural Science of China (No. R17F050003), National Key Basic Research Program of China (No. 2015CB352003), the Fundamental Research Funds for the Central Universities, the Program for Zhejiang Leading Team of S&T Innovation, the Cao Guangbiao Advanced Technology Program, and First-Class Universities and Academic Programs. C.F.K. acknowledges funding from the U.K. Engineering and Physical Sciences Research Council, EPSRC (grants EP/L015889/1 and EP/H018301/1), the Wellcome Trust (grants 3–3249/Z/16/Z and 089703/Z/09/Z) and the U.K. Medical Research Council, MRC (grants

MR/K015850/1 and MR/K02292X/1), MedImmune, and Infinitus (China) Ltd. This project has received funding from the European Union's Horizon 2020 research and innovation programme under Grant Agreement No. 722380.

Conflict of Interest

The authors declare no conflict of interest.

Keywords

frequency shifting and stitching, polygon planar waveguides, polymer fluorescent films, super-resolution imaging

Received: January 5, 2019

Revised: March 8, 2019

Published online:

-
- [1] S. W. Hell, J. Wichmann, *Opt. Lett.* **1994**, *19*, 780.
- [2] T. A. Klar, E. Engel, S. W. Hell, *Phys. Rev. E* **2001**, *64*, 066613.
- [3] B. Hein, K. I. Willig, S. W. Hell, *Proc. Natl. Acad. Sci. U. S. A.* **2008**, *105*, 14271.
- [4] E. Betzig, G. H. Patterson, R. Sougrat, O. W. Lindwasser, S. Olenych, J. S. Bonifacino, M. W. Davidson, J. Lippincott-Schwartz, H. F. Hess, *Science* **2006**, *313*, 1642.
- [5] S. T. Hess, T. P. K. Girirajan, M. D. Masony, *Biophys. J.* **2006**, *91*, 4258.
- [6] F. Ströhl, C. F. Kaminski, *Optica* **2016**, *3*, 667.
- [7] M. G. L. Gustafsson, *Proc. Natl. Acad. Sci. U. S. A.* **2005**, *102*, 13081.
- [8] M. J. Rust, M. Bates, X. W. Zhuang, *Nat. Methods* **2006**, *3*, 793.
- [9] M. Bates, B. Huang, G. T. Dempsey, X. W. Zhuang, *Science* **2007**, *317*, 1749.
- [10] L. Schermelleh, R. Heintzmann, H. Leonhardt, *J. Cell Biol.* **2010**, *190*, 165.
- [11] Z. Jacob, L. V. Alekseyev, E. Narimanov, *Opt. Express* **2006**, *14*, 8247.
- [12] Z. W. Liu, H. Lee, Y. Xiong, C. Sun, X. Zhang, *Science* **2007**, *315*, 1686.
- [13] J. Rho, Z. L. Ye, Y. Xiong, X. B. Yin, Z. W. Liu, H. Choi, G. Bartal, X. Zhang, *Nat. Commun.* **2010**, *1*, 143.
- [14] D. Lu, Z. W. Liu, *Nat. Commun.* **2012**, *3*, 1205.
- [15] Z. B. Wang, W. Guo, L. Li, B. Luk' yanchuk, A. Khan, Z. Liu, Z. C. Chen, M. H. Hong, *Nat. Commun.* **2011**, *2*, 218.
- [16] X. Hao, C. F. Kuang, X. Liu, H. J. Zhang, Y. H. Li, *Appl. Phys. Lett.* **2011**, *99*, 203102.
- [17] A. Darafsheh, G. F. Walsh, L. D. Negro, V. N. Astratov, *Appl. Phys. Lett.* **2012**, *101*, 141128.
- [18] X. Hao, X. Liu, C. F. Kuang, Y. H. Li, Y. L. Ku, H. J. Zhang, H. F. Li, L. M. Tong, *Appl. Phys. Lett.* **2013**, *102*, 013104.
- [19] X. W. Liu, C. F. Kuang, X. Hao, C. L. Pang, P. F. Xu, H. F. Li, Y. Liu, C. Yu, Y. K. Xu, D. Nan, W. D. Shen, Y. Fang, L. N. He, X. Liu, Q. Yang, *Phys. Rev. Lett.* **2017**, *118*, 076101.
- [20] C. L. Pang, X. W. Liu, M. H. Zhuge, X. Liu, M. G. Somekh, Y. Y. Zhao, D. Jin, W. D. Shen, H. F. Li, L. Wu, C. H. Wang, C. F. Kuang, Q. Yang, *Opt. Lett.* **2017**, *42*, 4569.
- [21] H. M. Grandin, B. Stadler, M. Textor, J. Voros, *Biosens. Bioelectron.* **2006**, *21*, 1476.
- [22] B. Agnarsson, A. B. Jonsdottir, N. B. Arnfinnsdottir, K. Leosson, *Opt. Express* **2011**, *19*, 22929.
- [23] B. Agnarsson, A. Lundgren, A. Gunnarsson, M. Rabe, A. Kunze, M. Mapar, L. Simonsson, M. Bally, V. P. Zhdanov, F. Höök, *ACS Nano* **2015**, *9*, 11849.
- [24] S. Ramachandran, D. A. Cohen, A. P. Quist, R. Lal, *Sci. Rep.* **2013**, *3*, 2133.
- [25] R. Diekmann, Ø. I. Helle, C. I. Øie, P. McCourt, T. R. Huser, M. Schüttelpelz, B. S. Ahluwalia, *Nat. Photonics* **2017**, *11*, 322.
- [26] M. Irie, T. Fukaminato, T. Sasaki, N. Tamai, T. Kawai, *Nature* **2002**, *420*, 759.
- [27] S. R. Forrest, *Nature* **2004**, *428*, 911.
- [28] L. P. Lu, D. Kabra, R. H. Friend, *Adv. Funct. Mater.* **2012**, *22*, 4165.
- [29] P. Jiang, M. J. McFarland, *J. Am. Ceram. Soc.* **2004**, *126*, 13778.
- [30] A. Endo, M. Ogasawara, A. Takahashi, D. Yokoyama, Y. Kato, C. Adachi, *Adv. Mater.* **2009**, *21*, 4802.
- [31] S. D. Kan, X. D. Liu, F. Z. Shen, J. Y. Zhang, Y. G. Ma, G. Zhang, J. C. Shen, *Adv. Funct. Mater.* **2003**, *13*, 603.
- [32] J. Chappell, D. G. Lidzey, P. C. Jukes, A. M. Higgins, R. L. Thompson, S. O'Connor, I. Grizzi, R. Fletcher, J. O'Brien, M. Geoghegan, A. L. Jones, *Nat. Mater.* **2003**, *2*, 616.
- [33] D. Kabra, L. P. Lu, M. H. Song, H. J. Snaith, R. H. Friend, *Adv. Mater.* **2010**, *22*, 3194.
- [34] M. Tountas, Y. Topal, M. Kus, M. Ersöz, M. Fakis, P. Argitis, M. Vasilopoulou, *Adv. Funct. Mater.* **2016**, *26*, 2655.
- [35] H. J. Bolink, E. Coronado, D. Repetto, M. Sessolo, E. M. Barea, J. Bisquert, G. Garcia-Belmonte, J. Prochazka, L. Kavan, *Adv. Funct. Mater.* **2008**, *18*, 145.
- [36] M. G. Gustafsson, *J. Microsc.* **2000**, *198*, 82.
- [37] E. Mudry, K. Belkebir, J. Girard, J. Savatier, E. Le Moal, C. Nicoletti, M. Allain, A. Sentenac, *Nat. Photonics* **2012**, *6*, 312.
- [38] J. Yang, L. Gong, Y. Shen, L. V. Wang, *Appl. Phys. Lett.* **2018**, *113*, 181104.
- [39] M. Saxena, G. Eluru, S. S. Gorthi, *Adv. Opt. Photonics* **2015**, *7*, 241.
- [40] J. Yang, L. Gong, X. Xu, P. Hai, Y. Shen, Y. Suzuki, L. V. Wang, *Nat. Commun.* **2017**, *8*, 780.
- [41] G. A. Zheng, R. Horstmeyer, C. H. Yang, *Nat. Photonics* **2013**, *7*, 735.
- [42] J. Yang, J. Li, S. He, L. V. Wang, *Optica* **2019**, *6*, 250.
- [43] J. S. Sun, Q. Chen, Y. Z. Zhang, C. Zuo, *Opt. Express* **2016**, *24*, 15765.
- [44] R. H. Friend, R. W. Gymer, A. B. Holmes, J. H. Burroughes, R. N. Marks, C. Taliani, D. D. C. Bradley, D. A. Dos Santos, J. L. BreÅdas, M. LoÈgdlund, W. R. Salaneck, *Nature* **1999**, *397*, 121.
- [45] Z. H. Nie, E. Kumacheva, *Nat. Mater.* **2008**, *7*, 277.
- [46] P. S. G. Pattader, I. Banerjee, A. Sharma, *Adv. Funct. Mater.* **2011**, *21*, 324.
- [47] Z. Bao, S. Campbell, *Thin Solid Films* **1999**, *352*, 239.
- [48] B. Agnarsson, S. Ingthorsson, T. Gudjonsson, K. Leosson, *Opt. Express* **2009**, *17*, 5075.